Journal of Materials Chemistry C

Scalable, Rapid, and Predictable Ultraviolet-Visible-Near-Infrared Camouflage Systems Inspired by Squid Skin

Journal:	*Journal of Materials Chemistry C*
Manuscript ID	TC-ART-10-2024-004209.R1
Article Type:	Paper
Date Submitted by the Author:	28-Feb-2025
Complete List of Authors:	Liu, Panyiming; University of California, Irvine, Department of Chemical Engineering and Materials Science Xu, Chengyi; Stanford University, Gorodetsky, Alon; University of California, Irvine, Department of Chemical Engineering and Materials Science

SCHOLARONE™
Manuscripts

Scalable, Rapid, and Predictable Ultraviolet-Visible-Near-Infrared Camouflage Systems Inspired by Squid Skin

Panyiming Liu,[1] Chengyi Xu,[1] Alon A. Gorodetsky[1,2*]

1. Department of Materials Science and Engineering, University of California, Irvine, Irvine, CA 92697, USA
2. Department of Chemical and Biomolecular Engineering, University of California, Irvine, Irvine, CA 92697, USA

*Correspondence to alon.gorodetsky@uci.edu

Abstract

Materials and systems with tunable optical and spectroscopic properties have attracted much research interest for applications in adaptive camouflage technologies. Within this context, our laboratory has developed bioinspired surface wrinkling-based adaptive camouflage technologies with tunable visible-to-infrared properties. Herein, we build upon these efforts and report the scalable fabrication of squid skin-inspired ultraviolet-visible-near-infrared adaptive camouflage systems with improved response times and predictable spectroscopic functionalities. These findings lay the groundwork for the iterative computational design, high-throughput manufacturing, and performance optimization of analogous adaptive camouflage, heat management, light-to-heat conversion, rewritable adaptive optics, and electromagnetic shielding platforms.

Introduction

Materials and systems with tunable optical and spectroscopic properties have attracted much research interest for applications in displays[1,2,3], sensors[4,5,6], anti-counterfeiting devices[7,8,9], photodetectors[10,11,12], biomedical instrumentation[13,14,15], information encryption methods[16,17,18], and camouflage systems[19,20,21]. Within this context, various mechanically- or electrically-controlled camouflage technologies that incorporate electrochromic materials, electroactive polymers, photonic gels, biomolecular films, microstructured layers, and/or two-dimensional nanomaterials have been reported to date.[22-33] Typically, such camouflage systems are fabricated by using procedures optimized over relatively small areas, which may not readily translate to the manufacturing high-performance systems over larger application-relevant areas[20,28,34,35]. Additionally, many camouflage systems are designed for functionality within the visible and/or infrared spectral ranges, with the same design approaches rarely remaining applicable within the ultraviolet spectral range[24,34,36,37]. Furthermore, the reported camouflage platforms' properties are not always easily simulated via computational models, with the lack of theoretical backing complicating optimization efforts and hindering fundamental understanding of the operating mechanisms[20,38,39]. Consequently, there has emerged powerful motivation for exploring the scalable large-area manufacturing, ultraviolet appearance-changing functionality, and computational modeling tractability of adaptive camouflage platforms.

Recently, our laboratory has developed surface wrinkling-based adaptive camouflage technologies with tunable visible-to-infrared properties[21,31,40,41] by drawing inspiration from the appearance-changing capabilities of cephalopods, such as the squid shown in **Fig. 1a**[42–45]. Specifically, we have looked to the unique hierarchical architecture of squid skin, wherein pigmented organs called chromatophores modulate the transmission of light by reversibly

expanding upon actuation[46-49] and reflective cells called iridophores modulate the reflection of light by reversibly changing ultrastructure upon actuation, as shown in **Fig. 1b**[49–52]. Accordingly, we have conceptualized parallel plate capacitor-type systems consisting of a spectroscopically-functional active layer, a deformable elastomeric membrane, and/or transparent proton-conducting electrodes, as shown in **Fig. 1c**[21,31,40,41]. Such systems simultaneously expand their areas, reconfigure their surface microstructure, and alter their interaction with incident light upon electrical or mechanical actuation, as shown in **Fig. 1c**[21,31,40,41]. Our general design paradigm has afforded cephalopod-inspired adaptive infrared-reflecting systems with amenability to patterning and multiplexing, stretchable multimodal infrared-transmitting platforms with multispectral functionality, micro- and nano-structured visible-to-infrared camouflage surfaces with hierarchically controlled morphologies, and ultraviolet-to-near-infrared signaling devices with outstanding operational stabilities (**Table S1**)[21,31,40,41]. Complementarily, other laboratories have leveraged controllable surface wrinkling for the development of infrared stealth structures, heat-managing selective emitters, light-to-heat conversion coatings, rewritable smart optics, thermochromic strain sensors, tunable optical cavities, and photothermal electromagnetic shielding (**Table S1**)[53-59]. However, despite significant progress, the prior combined work demonstrated some limitations related to dynamic tunability across multiple spectral bands, accurate prediction of the optical properties, rapid responsiveness upon repeated actuation, and scalable fabrication over large areas.

Herein, we report the scalable fabrication of squid skin-inspired ultraviolet-visible-near-infrared (UV-VIS-NIR) camouflage systems with improved response times and computationally predictable spectroscopic functionalities. Initially, we demonstrate the preparation of both small- and large-area dielectric elastomer actuator-type camouflage systems via a general fabrication

strategy. Subsequently, we investigate our small-area systems' visible, ultraviolet, and near-infrared appearance-changing capabilities and actuation-dependent metrics, characterize the reversible changes in the systems' surface morphologies and spectroscopic properties, and computationally model the systems' spectroscopic properties by leveraging the quantitative morphological characterization. Last, we analogously investigate, characterize, and model our large-area systems *via* the same general strategy. The resulting findings address challenges related to ultraviolet-to-near-infrared camouflage functionality, computational spectroscopic predictability, rapid responsiveness, and scalable fabrication for our camouflage systems and may guide similar advances for analogous surface wrinkling-based heat management, light-to-heat conversion, rewritable adaptive optics, and electromagnetic shielding technologies.

Results

We first prepared dielectric elastomer actuator-type devices via a general approach that accommodated scaling from small to large areas. Towards this end, we leveraged a multi-step process that adopted procedures previously reported for analogous device architectures (see **Fig. S1-S3** and the Methods for details)[21,31,40,41]. First, we equiaxially stretched optically transparent acrylate-based elastomer layers and mounted these layers onto circular or square frames to form a free-standing structure for device assembly (**Fig. S1a,b**, step i, **Fig. S2**, step i, and **Fig. S3**, step i). Second, we laminated two identical optically-transparent proton-conducting copolymer membrane electrodes onto both sides of the mounted elastomer layers to define the devices and their active regions (**Fig. S1a,b**, step ii, **Fig. S2**, step ii and **Fig. S3**, step ii). Third, we connected two conductive aluminum foil-based electrical leads to the laminated top and bottom proton-conducting electrodes to facilitate the application of bias to the devices (**Fig. S1a,b**, step iii, **Fig.**

S2, step iii, and **Fig. S3**, step iii). Fourth, we applied a bias of 3.8 kV between the electrodes in order to expand and thus pre-condition the devices' active regions (**Fig. S1a,b**, step iv, **Fig. S2**, step iv, and **Fig. S3**, step iv). Last, we removed the applied bias in order to not only contract but also simultaneously wrinkle the devices' active regions (**Fig. S1a,b**, step v, **Fig. S2**, step v, and **Fig. S3**, step v). The overall scalable fabrication procedure readily furnished devices with either small active regions (areas of ~ 0.8 cm^2 or ~ 4.9 cm^2) or large active regions (areas of ~ 113 cm^2).

We continued our efforts by studying the small-area devices' visible, ultraviolet, and near-infrared appearance-changing functionalities and actuation-dependent metrics. For this purpose, we visualized and quantified the visible appearances, ultraviolet contrasts, near-infrared contrasts, areal strains, response times, and cycling stabilities of small-area devices during electrical actuation under either visible, ultraviolet, or near-infrared light illumination with digital, ultraviolet, or near-infrared camera imaging, respectively (see **Fig. 2a** and the Methods for details). Under visible light, the devices' initially-smaller active regions were opaque before actuation but became almost completely transparent after areal expansion upon 3.8 kV actuation (**Fig. 2b** and **Video S1**). Under ultraviolet light, the devices' active regions were distinct from the background but became nearly indistinguishable from the background after areal expansion upon 3.8 kV actuation (**Fig. 2c** and **Video S2**). Under near-infrared light, the devices' active regions again stood out from the background but became almost identical to the background after areal expansion upon 3.8 kV actuation (**Fig. 2d** and **Video S3**). Notably, the small-area devices' active regions featured visible, ultraviolet, and near-infrared contrast changes with similar sigmoidal dependences on the actuation voltage and comparable maxima of - 60 ± 2%, - 51 ± 2%, and - 55 ± 2%, respectively, for 3.8 kV actuation (**Fig. S4**). Moreover, the small-area devices showcased areal strains that reached maxima of 59 ± 4% upon 3.8 kV actuation (**Fig. S5**), rapid response times with values as

low as 0.103 ± 0.006 s for a 2.0 Hz frequency (**Fig. S6**), and excellent stabilities across 500 consecutive 3.8 kV actuation cycles (**Fig. S7**). These experiments showed that our small-area devices not only possessed tandem visible, ultraviolet, and near-infrared camouflage capabilities but also rapid response times and excellent cycling stabilities, which is a relatively rare combination among analogous technologies.

We in turn investigated the mechanistic origins of our small-area devices' visible, ultraviolet, and near-infrared appearance-changing functionalities. For this purpose, we characterized and quantified the surface morphologies and spectroscopic properties of small-area devices before and after electrical actuation by using optical microscopy (OM), atomic force microscopy (AFM), and UV-VIS-NIR spectroscopy (see **Fig. 3a** and the Methods for details). Before actuation, the small-area devices' active regions were covered by sparsely-arranged interconnected wrinkles, which featured heights of 0.475 ± 0.038 μm, widths of 1.53 ± 0.07 μm, and separations of 10.1 ± 0.7 μm (**Fig. 3b**, left and **Table S2**). These unactuated devices displayed high total transmittances of 91 ± 2%, with specular and diffuse components of 67 ± 2% and 24 ± 1%, respectively (**Fig. 3c**, left and **Table S3**); low total reflectances of 9 ± 1%, with specular and diffuse components of 3 ± 1% and 6 ± 1%, respectively (**Fig**. **S8a,** left and **Table S3**); and comparatively negligible absorptances of < 1 % (**Fig. S8b**, left, and **Table S3**). After 3.8 kV actuation, the small-area devices' active regions were comparatively flat without obvious micron-scale wrinkles (**Fig. 3b**, right). These actuated devices displayed high total transmittances of 93 ± 1%, with specular and diffuse components of 92 ± 1% and 1 ± 1%, respectively (**Fig. 3c**, right and **Table S3**); low total reflectances of 8 ± 1%, with specular and diffuse components of 7 ± 1% and 1 ± 1%, respectively (**Fig. S8a**, right and **Table S3**); and comparatively negligible absorptances of < 1 % (**Fig. S8b**, right and **Table S3**). Although the devices' total transmittances and reflectances

remained relatively unchanged by actuation, their specular-to-diffuse transmittance ratios increased from 3 to 92 and specular-to-diffuse reflectance ratios increased from 0.5 to 7 upon actuation (**Fig. 3c**, **Fig. S8a**, and **Table S3**). Such relative changes in the devices' specular and diffuse transmittances and reflectances resulted from their transition between wrinkled and flattened states upon actuation, in agreement with literature precedent for analogous systems (**Fig. 3b,c**, **Fig. S8a**, and **Table S3**)[31,40,53]. These combined experiments indicated that our small-area devices' appearance-changing capabilities were driven by changes in their electrically-reconfigurable surface morphologies.

We subsequently sought to better understand the mechanistic origins of our small-area devices' visible, ultraviolet, and near-infrared appearance-changing functionalities and corresponding tunable spectroscopic properties. For this purpose, we numerically modeled the spectroscopic characteristics of small-area devices before and after electrical actuation by modifying an established approach reported for microstructured surfaces and leveraging our quantitative surface morphological characterization (see **Fig. S9**, **Table S2**, and the Methods for details)[60-63]. Before actuation, the small-area devices featured high simulated total transmittances of 91 ± 1%, with specular and diffuse components of 73 ± 3% and 18 ± 3%, respectively (**Fig. 3c**, left and **Table S3**); low simulated total reflectances of 9 ± 1%, with specular and diffuse components of 4 ± 1% and 5 ± 1%, respectively (**Fig. S8a**, left and **Table S3**); and comparatively negligible simulated absorptances of < 1 % (**Fig. S8b**, left, and **Table S3**). After actuation, the small-area devices featured high simulated total transmittances of 93%, with specular and diffuse components of 92% and 1%, respectively (**Fig. 3c**, right and **Table S3**); low total reflectances of 7%, with specular and diffuse components of 7% and 0%, respectively (**Fig. S8a**, right and **Table S3**); and comparatively negligible absorptances of < 1 % (**Fig. S8b**, right, and **Table S3**). Although

the devices' simulated total transmittances and reflectances were relatively unchanged by actuation, their specular-to-diffuse transmittance ratios increased from 4 to 92 and specular-to-diffuse reflectance ratios increased from 0.8 to > 7 after actuation (**Fig. 3c**, **Fig. S8a**, and **Table S3**). The agreement between our simulations and experiments reinforced the notion that the changes in our small-area devices' specular and diffuse transmittances and reflectances resulted from their transition between unactuated wrinkled and actuated flattened states (**Fig. 3b,c**, **Fig. S8a**, and **Table S3**). These simulations confirmed that our small-area devices' appearance-changing capabilities and tunable spectroscopic properties were dictated by their electrically-reconfigurable surface microstructures.

We further expanded our efforts by studying the large-area devices' visible, ultraviolet, and near-infrared appearance-changing functionalities and their actuation-dependent metrics. For this purpose, we visualized and quantified the visible appearances, ultraviolet contrasts, near-infrared contrasts, areal strains, response times, and cycling stabilities of large-area devices during electrical actuation under either visible, ultraviolet, or near-infrared light illumination with digital, ultraviolet, or near-infrared camera imaging, respectively (see **Fig. 4a** and the Methods for details). Under visible light, the devices' originally-smaller active regions were opaque before actuation but became more transparent after areal expansion upon 3.8 kV actuation (**Fig. 4b** and **Video S4**). Under ultraviolet light, the devices' active regions were distinct from the background but became nearly indistinguishable from the background after areal expansion upon 3.8 kV actuation (**Fig. 4c** and **Video S5**). Under near-infrared light, the devices' active regions stood out from the background but became almost identical to the background after areal expansion upon 3.8 kV actuation (**Fig. 4d** and **Video S6**). Notably, the large-area devices' active regions featured visible, ultraviolet, and near-infrared contrast changes with similar sigmoidal dependences on the actuation

voltage and comparable maxima of - 28 ± 2%, - 26 ± 2%, and - 26 ± 2%, respectively, for 3.8 kV actuation (**Fig. S10**). Moreover, the large-area devices featured areal strains that reached maxima of 25 ± 1% upon 3.8 kV actuation (**Fig. S11**), rapid response times with values as low as 0.128 ± 0.010 s for a 2.0 Hz frequency (**Fig. S12**), and good stabilities across 500 consecutive 3.8 kV actuation cycles (**Fig. S13**). These experiments showed that our devices generally maintained their tandem visible, ultraviolet, and near-infrared camouflage capabilities, rapid response times, and excellent cycling stabilities even when they were scaled to much larger areas.

We in turn investigated the mechanistic origins of our large-area devices' visible, ultraviolet, and near-infrared appearance-changing functionalities. For this purpose, we characterized and quantified the surface morphologies and spectroscopic properties of large-area devices before and after electrical actuation by using OM, AFM, and UV-VIS-NIR spectroscopy (see **Fig. 5a** and the Methods for details). Before actuation, the large-area devices' active regions were covered by sparsely-distributed interconnected wrinkles, which featured heights of 0.343 ± 0.049 μm, widths of 1.55 ± 0.16 μm, and separations of 14.9 ± 1.6 μm (**Fig. 5b**, left and **Table S2**). These unactuated devices showcased high total transmittances of 90 ± 2%, with specular and diffuse components of 74 ± 2% and 16 ± 1%, respectively (**Fig. 5c**, left and **Table S3**); low total reflectances of 9 ± 1%, with specular and diffuse components of 4 ± 1% and 5 ± 1%, respectively (**Fig. S14a**, left and **Table S3**); and relatively negligible absorptances of < 1 % (**Fig. S14b**, left, and **Table S3**). After 3.8 kV actuation, the large-area devices' active regions were relatively flat without apparent micron-scale wrinkles (**Fig. 5b**, right). These actuated devices displayed high total transmittances of 93 ± 1%, with specular and diffuse components of 92 ± 1% and 1 ± 1%, respectively (**Fig. 5c**, right and **Table S3**); low total reflectances of 9 ± 1%, with specular and diffuse components of 8 ± 1% and 1 ± 1%, respectively (**Fig. S14a**, right and **Table S3**); and

relatively negligible absorptances of < 1% (**Fig. S14b**, right, and **Table S3**). Although the devices' total transmittances and reflectances remained relatively unchanged by actuation, their specular-to-diffuse transmittance ratios increased from 5 to 92 and specular-to-diffuse reflectance ratios increased from 0.8 to 8 upon actuation (**Fig. 5c**, **Fig. S14a**, and **Table S3**). Such relative changes in the devices' specular and diffuse transmittances and reflectances resulted from their transition between wrinkled and flattened states upon actuation, in agreement with literature precedent for analogous systems (**Fig. 5b,c**, **Fig. S14a**, and **Table S3**)[31,40,53]. These combined experiments indicated that our devices' appearance-changing capabilities remained driven by changes in their electrically-tunable surface morphologies even when they were scaled to much larger areas.

We subsequently sought to better understand the mechanistic origins of our large-area devices' visible, ultraviolet, and near-infrared appearance-changing functionalities and corresponding tunable spectroscopic properties. For this purpose, we numerically modeled the spectroscopic characteristics of large-area devices before and after electrical actuation by modifying an established approach reported for microstructured surfaces and incorporating our quantitative surface morphological characterization (see **Fig. S9**, **Table S2**, and the Methods for details)[60-63]. Before actuation, the large-area devices exhibited high simulated total transmittances of 92 ± 1%, with specular and diffuse components of 83 ± 3% and 9 ± 3%, respectively (**Fig. 5c**, left and **Table S3**); low simulated total reflectances of 8 ± 1%, with specular and diffuse components of 6 ± 1% and 2 ± 1%, respectively (**Fig. S14a**, left and **Table S3**); and relatively negligible simulated absorptances of < 1% (**Fig. S14b**, left and **Table S3**). After actuation, the large-area devices exhibited high simulated total transmittances of 93%, with specular and diffuse components of 92% and 1%, respectively (**Fig. 5c**, right and **Table S3**); low total reflectances of 7%, with specular and diffuse components of 7% and 0%, respectively (**Fig. S14a**, right and **Table**

S3); and relatively negligible absorptances of < 1 % (**Fig. S14b**, left, and **Table S3**). Although the devices' simulated total transmittances and reflectances were relatively unchanged by actuation, their specular-to-diffuse transmittance ratios increased from 9 to 92 and specular-to-diffuse reflectance ratios increased from 3 to > 7 after actuation (**Fig. 5c** and **Fig. S14a**, and **Table S3**). The agreement between our simulations and measurements further reinforced the notion that the large-area devices' specular and diffuse transmittances and reflectances resulted from their transition between unactuated wrinkled and actuated flattened states (**Fig. 5b,c**, **Fig. S14a**, and **Table S3**). These combined simulations confirmed that our devices' appearance-changing capabilities and tunable spectroscopic properties were dictated by their electrically-reconfigurable surface microstructures even when they were scaled to larger areas.

Conclusion

In summary, we have demonstrated the scalable fabrication of dielectric elastomer actuator-type camouflage systems, explored the dynamic functionalities of such systems within the UV-VIS-NIR spectral range, and validated the computational prediction of these systems' tunable spectroscopic properties. These combined findings hold significance for multiple reasons. First, our modular fabrication approach requires inexpensive commercial materials, employs a limited number of straightforward steps, and can proceed entirely on a benchtop, with the large-area devices generally resembling their small-area counterparts and featuring among the largest areas reported for comparable systems (**Table S1**). Such production modularity may enable consideration of our devices in camouflage applications where their sizes are sufficient to counterbalance the large actuation/switching voltages, and the described generalizable benchtop procedures could potentially help improve the fabrication of wrinkled surfaces for other

applications. Second, our small-area and large-area devices feature camouflage capabilities with competitive figures of merit, including notable response times of < 0.130 s, repeatable functionality over at least 500 consecutive cycles, and specular-to-diffuse UV-VIS-NIR transmittance ratio modulation of ~ 18- to ~ 30-fold (**Table S1**). Such good quantitative metrics for our devices are especially noteworthy when considering their tandem appearance-changing functionality across multiple spectral bands, and they highlight the generalizability of the devices' underlying operating mechanism, which relies upon reversible changes in surface morphology. Third, our computational methodology faithfully captures the small-area and large-area devices' UV-VIS-NIR spectroscopic properties, i.e., their total, specular, and diffuse reflectances and transmittances, while requiring only readily-measurable morphology/thickness information and standard optical constants as input parameters (**Tables S2** and **S3**). Such advantageous computational tractability opens the possibility of designing and optimizing our camouflage systems entirely *in silico* with reasonable accuracy, thereby potentially accelerating prototyping in the future, and our general approach should translate to the development of analogous optically- and spectroscopically-active surface wrinkling-based systems. Altogether, these findings lay the groundwork for the iterative computational design, high-throughput manufacturing, and performance optimization of our adaptive camouflage systems and may guide similar advances for heat management, light-to-heat conversion, rewritable adaptive optics, electromagnetic shielding, and other technologies that leverage tunable surface wrinkling.

Methods

Fabrication of the Devices. The small-area and large-area devices were fabricated by adopting and modifying established protocols[21,31,40,41]. The fabrication procedure was performed on a

benchtop from commercially available materials. First, small-area or large-area acrylate-based dielectric elastomer membranes (VHB 4905, 3M) were equiaxially stretched by 1,600% or 1,300% (relative to their initial areas) and mounted onto rigid circular or square acrylic frames featuring internal diameters of either 2.5 and 4 cm or 20 cm, respectively. Second, small-area or large-area proton-conducting sulfonated pentablock copolymer electrodes (NEXAR™, Kraton Polymers LLC) with rectangular extensions and active region diameters of either 1 and 2.5 cm or 12 cm, respectively, were laminated onto opposing sides of the mounted membranes. Third, two identical rectangular aluminum foil (Reynolds) electrical leads were connected to the opposing proton-conducting copolymer electrodes, completing the tri-layer architectures. Fourth, a voltage of 3.8 kV was applied between the electrodes for a duration of 20 s to expand the active areas of the small-area and large-area devices. Last, the applied voltage was removed to contract the active areas of the small-area and large-area devices. The completed devices were used for electrical actuation, digital camera imaging, ultraviolet camera imaging, near-infrared camera imaging, OM, AFM, and UV-VIS-NIR spectroscopy characterization.

Electrical Actuation of the Devices. The small-area and large-area devices were electrically actuated by following reported protocols[21,31,40,41]. The devices were actuated with a home-built high-voltage power source consisting of a Stanford Research DS 345 function generator, a Texas Instruments OPA 548 operational amplifier, and an EMCO E80 high-voltage converter. The devices were simultaneously imaged with either an Apple iPhone built-in digital camera or with a Canon PowerShot SX520 digital single-lens reflex camera throughout actuation. The measurements were performed under room lighting illumination above a black benchtop background in ambient atmosphere at room temperature. The devices' areal strains resulting from

actuation with various voltages at different frequencies were calculated from the obtained videos and images according to the equation:

$$areal\ strain = (A_1 - A_0)/A_0 \quad (1)$$

where A_0 is the area of the active region obtained from device images before electrical actuation and A_1 is the area of the active region obtained from device images after electrical actuation. The devices' response times during typical actuation cycles at different frequencies were calculated from the obtained videos according to the equation:

$$response\ time = t_{90\%} - t_{10\%} \quad (2)$$

where $t_{90\%}$ is the rise time required to reach 90% of the maximum device area change during a typical actuation cycle and $t_{10\%}$ is the rise time required to reach 10% of the maximum device area change during the same actuation cycle. The various electrical actuation experiments were all repeated for at least three independent small-area and large-area devices. The videos and images were processed and analyzed with the Premiere (Adobe), Photoshop (Adobe), and Origin 8.5 (OriginLab) software packages.

Digital Camera Imaging of the Devices. The small-area and large-area devices' visible appearances were characterized by adopting and modifying reported protocols[21,31,40,41]. The devices were imaged with a Canon PowerShot SX520 digital single-lens reflex camera. The measurements were performed under room lighting illumination above a black benchtop background in ambient atmosphere at room temperature. The devices' visible contrast changes were calculated from the obtained videos and images according to the following equation[41,64]:

$$visible\ contrast\ change = \frac{final\ state\ image\ pixel\ values - initial\ state\ image\ pixel\ values}{initial\ state\ image\ pixel\ values} \quad (3)$$

where the image pixel values for the final (actuated) state and the image pixel values for the initial (unactuated) states were auto-generated from the corresponding images' RGB channels by using

the built-in histogram function in the Photoshop (Adobe). The digital camera imaging experiments were repeated for at least three independent small-area and large-area devices. The videos and images were processed and analyzed with the Photoshop (Adobe) and Origin 8.5 (OriginLab) software packages.

Ultraviolet Camera Imaging of the Devices. The small-area and large-area devices' ultraviolet appearances were characterized by adopting and modifying reported protocols[21,31,40,41]. The devices were imaged with an Urgaze UVLOOK ultraviolet camera with a built-in ultraviolet illumination source. The measurements were performed under ultraviolet illumination above a black cloth background in ambient atmosphere at room temperature. The devices' ultraviolet contrast changes were calculated from the obtained videos and images according to the following equation[41,64]:

$$ultraviolet\ contrast\ change = \frac{final\ state\ image\ pixel\ values - initial\ state\ image\ pixel\ values}{initial\ state\ image\ pixel\ values} \quad (4)$$

where the image pixel values for the final (actuated) state and the image pixel values for the initial (unactuated) state were auto-generated from the corresponding images' luminosity channels by using the built-in histogram function in Adobe Photoshop. The ultraviolet camera imaging experiments were repeated for at least three independent small-area and large-area devices. The videos and images were processed and analyzed with the Photoshop (Adobe) and Origin 8.5 (OriginLab) software packages.

Near-Infrared Camera Imaging of the Devices. The small-area and large-area devices' near-infrared appearances were characterized by adopting and modifying reported protocols[21,31,40,41]. The devices were imaged with an ORDRO AE20 near-infrared camera with a built-in near-infrared illumination source. The measurements were performed under near-infrared illumination above a black cloth background in ambient atmosphere at room temperature. The devices' near-infrared

contrast changes were calculated from the obtained videos and images according to the following equation[41,64]:

$$near\ infrared\ contrast\ change = \frac{final\ state\ image\ pixel\ values - initial\ state\ image\ pixel\ values}{initial\ state\ image\ pixel\ values} \quad (5)$$

where the image pixel values for the final (actuated) state and the image pixel values for the initial (unactuated) state were auto-generated from the corresponding images' luminosity channels by using the built-in histogram function in Adobe Photoshop. The near-infrared camera imaging experiments were repeated for at least three independent small-area and large-area devices. The videos and images were processed and analyzed with the Photoshop (Adobe) and Origin 8.5 (OriginLab) software packages.

OM Characterization of the Devices. The small-area and large-area devices' microscale morphologies were qualitatively characterized by following reported protocols[21,40]. The devices were characterized with a Thermo Fisher Scientific EVOS™ M5000 microscope imaging system. The measurements were performed in transmission mode by using a 40X objective under ambient conditions at room temperature. The measurements were performed for devices that were secured with tape to prevent elastomer contraction or morphological changes. The OM characterization was repeated for at least three independent unactuated and actuated small-area devices and large-area devices. The images were processed and analyzed with the Photoshop (Adobe) software package.

AFM Characterization of the Devices. The small-area and large-area devices' microscale morphologies were qualitatively and quantitatively characterized by following reported protocols[31,40,41]. The devices were characterized with an Asylum Cypher ES environmental atomic force microscope. The measurements were performed in tapping mode by using an Olympus AC55TS microcantilever under ambient conditions at room temperature. The measurements were

performed for devices that were secured with tape to prevent elastomer contraction or morphological changes, attached to silicon substrates, and mounted onto disc-shaped AFM sample holders (Ted Pella). The average wrinkle height $H_{wrinkle}$ was calculated from the images obtained before actuation according to the following equation:

$$H_{wrinkle} = H_w - H_f \quad (5)$$

where the heights of the wrinkles H_w were estimated by masking out the flat regions using the Threshold function in ImageJ and the heights of the flat regions H_f were estimated by masking out the wrinkles using the Threshold function in ImageJ. The average wrinkle width $W_{wrinkle}$ was calculated from the images obtained before actuation according to the following equation:

$$W_{wrinkle} = \frac{A_w}{L_w} \quad (6)$$

where the areas of the wrinkles A_w were estimated by using the Threshold function in ImageJ and the lengths of the wrinkles L_w were estimated by using the Segmented Line function in ImageJ. The average wrinkle peak-to-peak distance range $D_{wrinkle}$ was calculated from the images obtained before actuation by extracting the Feret's diameters by using the Analyze Particle function in ImageJ. The AFM characterization was repeated for at least three independent unactuated and actuated small-area and large-area devices. The images were processed and analyzed with the Gwyddion (Czech Metrology Institute) and ImageJ (National Institutes of Health) software package.

UV-VIS-NIR Spectroscopy Characterization of the Devices. The small-area and large-area devices' spectroscopic properties were quantitatively characterized by following reported protocols[21,31,40,41]. The measurements were performed with a Jasco V670 UV-VIS-NIR Spectrophotometer outfitted with a Jasco ILN-925 150 mm integrating sphere. The total and diffuse transmittance measurements were performed in transmission mode at normal incidence

between wavelengths of 300 nm and 2.0 μm by using a rectangular-shaped port with a length of 0.9 cm and a width of 1.3 cm, and the total and diffuse reflectance measurements were performed in reflection mode at a 5° incidence angle between wavelengths of 300 nm and 2.0 μm by using a square-shaped port with a width and length of 1.6 cm under ambient conditions at room temperature. The measurements were performed for devices with ~ 4.9 cm^2 active regions, which were sufficient to fully cover the ports. The measurements were performed for devices that were secured with tape to prevent elastomer contraction or morphological changes. The measurements were referenced to Jasco Spectralon standards for accurate calibration and calculation of the total, specular, and diffuse transmittances and reflectances. The absorptance A was calculated from the obtained spectra according to the standard equation[65,66]:

$$A + T_{total} + R_{total} = 1 \quad (7)$$

where T_{total} is the measured total transmittance and R_{total} is the measured total reflectance.

The specular transmittance $T_{specular}$ was calculated according to the standard equation[65,66]:

$$T_{specular} = T_{total} - T_{diffuse} \quad (8)$$

where $T_{diffuse}$ is the measured diffuse transmittance.

The specular reflectance $R_{specular}$ was calculated according to the standard equation[65,66]:

$$R_{specular} = R_{total} - R_{diffuse} \quad (9)$$

where $R_{diffuse}$ is the measured diffuse reflectance. The UV-VIS-NIR spectroscopy measurements were repeated for at least three independent unactuated and actuated small-area devices and large-area devices. The spectra were processed and analyzed with the Jasco Spectra Manager™ Suite (Jasco) and Origin 8.5 (OriginLab) software packages.

Simulation of the UV-VIS-NIR Spectroscopic Properties of the Devices. The small-area and large-area devices' spectroscopic properties were computationally modeled by adopting and

modifying established protocols[60-63,67]. The modeling was performed by using the Electromagnetic Waves, Frequency Domain Interface in the Wave Optics Module of the COMSOL Multiphysics 5.6 (COMSOL) software[62]. The total, specular, and diffuse transmittance; total, specular, and diffuse reflectance; and absorptance calculations between wavelengths of 300 nm and 2.0 μm were performed by considering the reflection, transmission, and absorption of incident light for the top and bottom interfaces of a two-dimensional unit cell and by using input parameters that approximated the physical characteristics of the tri-layer devices. The two-dimensional unit cell consisted of top and bottom interfaces from sulfonated pentablock copolymer (SPC) and acrylate-based dielectric elastomer structures covered with periodic uniformly-distributed idealized wrinkles (**Fig. S9**). The two-dimensional unit cell used Floquet periodic boundary conditions, which ensured an identical continuous geometry; Monitoring boundaries, which enabled calculation of the total transmittance and reflectance; Port boundary conditions, which enabled internal generation of incident light and calculation of the specular transmittance and reflectance; and Perfectly matched layers, which absorbed all reflected and transmitted light (**Fig. S9**). The geometric input parameters included 1) the measured SPC layer thickness Th_{SPC}; 2) the measured wrinkle height range $H_{wrinkle}$; 3) the measured wrinkle width range $W_{wrinkle}$; and 4) the measured wrinkle peak-to-peak distance range $D_{wrinkle}$ (i.e., unit cell width) (**Table S2**). The optical input parameters included 1) the measured SPC refractive index $\overline{n}_{SPC}$; 2) the reported acrylate-based dielectric elastomer refractive index $\overline{n}_{acrylate}$; and 3) the reported air refractive index $\overline{n}_{air}$ (**Table S2**)[68,69]. The total transmittance $T_{total,sim}$ was calculated from the simulated spectra according to the following equation[60,70]:

$$T_{total,sim} = \frac{T_{top}T_{bottom}}{1-R_{top}R_{bottom}} \quad (10)$$

where T_{top} is the computed total transmittance for the top interface, T_{bottom} is the computed total transmittance for the bottom interface, R_{top} is the computed total reflectance for the top interface, and R_{bottom} is the computed total reflectance for the bottom interface. The total reflectance $R_{total,sim}$ was calculated from the simulated spectra according to the following equation[60,70]:

$$R_{total,sim} = R_{top} + \frac{R_{bottom}{T_{top}}^2}{1-R_{top}R_{bottom}} \quad (11)$$

The absorptance $A_{total,sim}$was calculated from the obtained spectra according to equation (7). The specular transmittance $T_{specular,\,sim}$ was calculated from the simulated spectra for the limiting case where the transmittance is much greater than the reflectance and absorptance according to the following equation[60,65,66,70]:

$$T_{specular,sim} = T_{specular,top}T_{specular,bottom} \quad (12)$$

where $T_{specular,top}$ is the computed specular transmittance for the top interface and $T_{specular,bottom}$ is the computed specular transmittance for the bottom interface. The diffuse transmittance $T_{diffuse,\,sim}$ was calculated from the obtained spectra according to equation (8). The specular transmittance $R_{specular,\,sim}$ was calculated from the simulated spectra according to the following equation[60,65,66,70]:

$$R_{specular,sim} = R_{specular,top} + R_{specular,bottom}{T_{specular,top}}^2 \quad (13)$$

where $R_{specular,top}$ is the computed specular reflectance for the top interface and $R_{specular,bottom}$ is the computed specular reflectance for the bottom interface. The diffuse reflectance $R_{diffuse,\,sim}$ was calculated from the obtained spectra according to equation (9). The average total reflectance, transmittance, and absorptance; specular transmittance and reflectance; diffuse transmittance and reflectance with associated standard deviations were calculated from spectra simulated over the wavelength range of 300 nm and 2.0 μm for the wrinkle geometry ranges corresponding to the

measured average values plus or minus one standard deviation (**Table S2** and **S3**). The spectra were processed and analyzed with the Origin 8.5 (OriginLab) software package.

Author contributions

A.A.G. supervised the research. A.A.G., P.L., and C.X. conceived the idea and designed the experiments. P.L. and C.X. fabricated and characterized the devices. P.L. developed and performed the computational simulations. P.L. analyzed and interpreted the measured and simulated data. P.L. and A.A.G. prepared the figures and wrote the manuscript. All authors discussed the results.

Conflicts of interest

C.X. and A.A.G. are listed as inventors on patent US11977207B2, which is related to the findings in this manuscript.

Acknowledgments

The authors are grateful to the Defense Advanced Research Projects Agency (cooperative agreements W911NF-16-2-0077 and D16AP00034 to A.A.G.) and the Office of Naval Research (grants N00014-17-1-2564 and N00014-21-1-2143 to A.A.G.) for their financial support. The authors thank Dr. Doron Kam for valuable discussions. The authors also thank the Laser Spectroscopy Laboratories (LSL) at the University of California, Irvine, for the use of their equipment and resources.

References

1. H. Sasabe and J. Kido, *Chem. Mater.*, 2011, **23**, 621–630.
2. L. Shao, X. Zhuo and J. Wang, *Adv. Mater.*, 2018, **30**, 1704338.
3. C. Ríos, P. Hosseini, R. A. Taylor, and H. Bhaskaran, *Adv. Mater.*, 2016, **28**, 4720-4726.
4. J.-M. Kim, C. Lee, Y. Lee, J. Lee, S.-J. Park, S. Park and J.-M. Nam, *Adv. Mater.*, 2021, **33**, 2006966.
5. M. Qin, M. Sun, M. Hua and X. He, *Curr. Opin. Solid State Mater. Sci.*, 2019, **23**, 13–27.
6. Q. Zhang, S. Niu, L. Wang, J. Lopez, S. Chen, Y. Cai, R. Du, Y. Liu, J.-C. Lai, L. Liu, C.-H. Li, X. Yan, C. Liu, J. B.-H. Tok, X. Jia and Z. Bao, *Adv. Mater.*, 2018, **30**, 1801435.
7. W. Hong, Z. Yuan and X. Chen, *Small*, 2020, **16**, 1907626.
8. Y. Sun, X. Le, S. Zhou and T. Chen, *Adv. Mater.*, 2022, **34**, 2201262.
9. X. Lai, Q. Ren, F. Vogelbacher, W. E. I. Sha, X. Hou, X. Yao, Y. Song and M. Li, *Adv. Mater.*,2022, **34**, 2107243.
10. C. Xie and F. Yan, *Small*, 2017, 13, 1701822.
11. S. Cai, X. J. Xu, W. Yang, J. X. Chen and X. S. Fang, *Adv. Mater.*, 2019, **31**, 1808138.
12. N. Zhang, Z. Lin, Z. Wang, S. Zhu, D. Chen, H. Qi and W. Zheng, *ACS Nano*, 2024, **18** (1), 652-661.
13. G. Hong, A. L. Antaris and H. Dai, *Nat. Biomed. Eng.*, 2017, **1**, 0010.
14. G. H. Lee *et al.*, *Nat. Rev. Mater.*, 2020, **5**, 149–165.
15. M. Jorfi, M. N. Roberts, E. J. Foster and C. Weder, *ACS Appl. Mater. Interfaces*, 2013, **5** (4), 1517-1526.
16. A. O. Omoniyi *et al.*, *Mater. Today Commun.*, 2023, **36**, 106508.
17. Y. Wu, X. Chen and W. Wu, *Small*, 2023, **19**, 2206709.

18. Q. Wang, B. Lin and M. Chen *et al.*, *Nat. Commun.*, 2022, **13**, 4185.

19. Y. Qiao, Z. Meng, P. Wang and D. Yan, *Front. Mater.*, 2021, **8**, 1–10.

20. L. M. Degenstein, D. Sameoto, J. D. Hogan, A. Asad and P. I. Dolez, *Micromachines*, 2021, **12**, 773.

21. C. Xu, G. T. Stiubianu and A. A. Gorodetsky, *Science*, 2018, **359**, 1495-1500.

22. H. Fu *et al.*, *Mater. Chem. Front.*, 2023, **7**, 2337-2358.

23. Z. Wu, Q. Zhao, X. Luo, H. Ma, W. Zheng, J. Yu, Z. Zhang, K. Zhang, K. Qu, R. Yang, N. Jian, J. Hou, X. Liu, J. Xu and B. Lu, *Chem. Mater.* 2022, **34** (22), 9923–9933.

24. N. Kamely, *J. Electron. Mater.*, 2022, **51**, 953–965.

25. E. G. C. Ergun and B. B. Carbas, *ChemistrySelect*, 2023, **8**, e202303463.

26. M. Faustini, *J. Sol-Gel Sci. Technol.*, 2020, **95**, 504–516.

27. M. A. Haque, K. Mito, T. Kurokawa, T. Nakajima, T. Nonoyama, M. Ilyas and J. Gong, *ACS Omega*, 2018, **3** (1), 55-62.

28. R. Xiong et al., *Chem. Soc. Rev.*, 2020, **49**, 983-1031.

29. L. Phan, W. G. Walkup IV, D. D. Ordinario, E. Karshalev, J.-M. Jocson, A. M. Burke and A. A. Gorodetsky, *Adv. Mater*., 2013, **25**, 5621-5625.

30. S. Dou, H. Xu, J. Zhao, K. Zhang, N. Li, Y. Lin, L. Pan and Y. Li, *Adv. Mater.*, 2021, **33**, 2000697.

31. C. Xu, M. Colorado Escobar and A. A. Gorodetsky, *Adv. Mater.*, 2020, **32**, 1905717.

32. X. Fan, S. Li, W. Zhang and W. Xu, *Ceram. Int.*, 2023, **49**, 5559–5572.

33. L. Liang, X. Yang, C. Li, R. Yu, B. Zhang, Y. Yang and G. Ji, *Adv. Mater.*, 2024, **36**, 2313939.

34. S. Tadepalli, J. M. Slocik, M. K. Gupta, R. R. Naik and S. Singamaneni, *Chem. Rev.*, 2017, **117**, 12705–12763.

35. Y. Gong, H. Wang, J. Luo, J. Chen and Z. Qu, *Materials*, 2024, **17**, 2564.

36. R. J. Denning, in *Engineering of High Performance Textiles*, ed. M. Miao, J. H. Xin, Elsevier, 2018, pp. 349-375.

37. H. Liu, L. Yu, B. Zhao, Y. Ni, P.g Gu, H. Qiu, W. Zhang and K. Chen, J. *Mater. Chem. C*, 2023, **11**, 285-298.

38. D. E. McCoy, A. V. Shneidman, A. L. Davis and J. Aizenberg, *Micron*, 2021, **151**, 103160.

39. J. Zhang, P. Wang, W. Xie, H. Wang, Y. Zhang and H. Zhou, *ACS Nano*, 2024, **18**, 24741−24769.

40. Y. Liu, Z. Feng, C. Xu, A. Chatterjee and A. A. Gorodetsky, *ACS Nano*, 2021, **15**, 17299–17309.

41. P. Pratakshya, C. Xu, D. J. Dibble, A. Mukazhanova, P. Liu, A. M. Burke, R. Kurakake, R.Lopez, P. R. Dennison, S. Sharifzadeh and A. A. Gorodetsky, *Nat. Commun*. 2023, **14**, 8528.

42. R. T. Hanlon and J. B. Messenger, *Cephalopod Behaviour*, Cambridge Univ. Press, 2nd ed., 2018.

43. L. M. Mathger, E. J. Denton, N. J. Marshall and R. T. Hanlon, *J. R. Soc. Interface*, 2009, **6**, S149−S163.

44. L. Phan, R.Kautz, E. M. Leung, K. L. Naughton, Y. V. Dyke and A. A. Gorodetsky, *Chemistry of Materials*, 2016, **28** (19), 6804-6816.

45. SD Diver Art, https://www.youtube.com/watch?v=0DBexhP1xQE, (accessed July 2024).

46. G. R. R. Bell, A. M. Kuzirian, S. L. Senft, L. M. Mäthger, T. J. Wardill and R.T. Hanlon, *Invertebr Biol*, **132**, 120-132.

47. T. L. Williams *et al.*, *Nat. Commun*., 2019, **10**, 1004.

48. J. B. Messenger, *Biol. Rev. Camb. Philos. Soc.* 2001, **76**, 473–528.

49. L. M. Mathger and R. T. Hanlon, *Cell Tissue Res.*, 2007, **329**, 179-186.

50. T. J. Wardill, P. T. Gonzalez-Bellido, R. J. Crook and R. T. Hanlon, *Proc. Biol. Sci.*, 2012, **279**, 4243-4252.

51. D. G. DeMartini, D. V. Krogstad and D. E. Morse, *Proc. Natl. Acad. Sci. U. S. A.*, 2013, **110**, 2552-2556.

52. D. G. DeMartini, M. Izumi, A. T. Weaver, E. Pandolfi and D. E. Morse, *J. Biol. Chem.*, 2015, **290** (24), 15238−15249.

53. J. Wang, Y. Li and J. Cui *et al.*, *Nanoscale Res. Lett.*, 2018, **13**, 361.

54. M. Sala-Casanovas, A. Krishna, Z. Yu and J. Lee, *Nanoscale Microscale Thermophys. Eng.*, 2019, **23** (3), 173-187.

55. K. R. Li, T.-H. Chang, Z. P. Li, H. T. Yang, F. F. Fu, T. T. Li, J. S. Ho and P.-Y. Chen, *Adv. Energy Mater.*, 2019, **9**, 1901687.

56. B. Jiang, L. Liu, Z. Gao, Z. Feng, Y. Zheng and W. Wang, *ACS Appl. Mater. Interfaces*, 2019, **11** (43), 40406-40415.

57. G. Lee, G. Y. Bae, J. H. Son, S. Lee, S. W. Kim, D. Kim, S. G. Lee and K. Cho, *Adv. Sci.* 2020, **7**, 2001184.

58. P. Güell-Grau, F. Pi, R. Villa, O. Eskilson, D. Aili, J. Nogués, B. Sepúlveda and M. Alvarez, *Adv. Mater.* 2022, **34**, 2106731.

59. R. Yu, L. Liang, Y. Zhao and G. Ji, *J. Mater. Chem. A*, 2024, **12**, 3923-3932.

60. E. Nichelatti, *J. Opt A: Pure Appl. Opt.*, 2002, **4**, 400–403.

61. W. Frei, https://www.comsol.com/blogs/how-to-model-the-optical-properties-of-rough-surfaces, (accessed July 2024).

62. Comsol Documentation, https://doc.comsol.com/5.6/doc/com.comsol.help.woptics/WaveOpti

csModuleUsersGuide.pdf, (accessed July 2024).

63. Comsol Application Gallery, https://www.comsol.com/model/plasmonic-wire-grating-wave-optics-14705, (accessed July 2024).
64. Adobe Documentation, https://helpx.adobe.com/photoshop/ using/viewing-histograms-pixel-values.html, (accessed July 2024).
65. B. E. A. Saleh and M. C. Teich, *Fundamentals of Photonics*, John Wiley & Sons, Inc., 1991.
66. A. Höpe, in *Experimental Methods in the Physical Sciences*, ed. T. A. Germer, J. C. Zwinkels, B. K. Tsai, Elsevier, 2014, pp. 179-219.
67. P. Liu, E. M. Leung, M. A. Badshah, C. S. Moore and A. A. Gorodetsky, *APL Bioeng*., 2023, **7**, 046111.
68. X. Zhang, J. Qiu, X. Li, J. Zhao and L. Liu, *Appl. Opt.*, 2020, **59**, 2337-2344.
69. P. E. Ciddor, *Appl. Opt.*, 1996, **35**, 1566–1573.
70. H. G. Hecht, *J. Res. Natl. Bur. Stand., Sect. A,* 1976, **80**, 567-583.

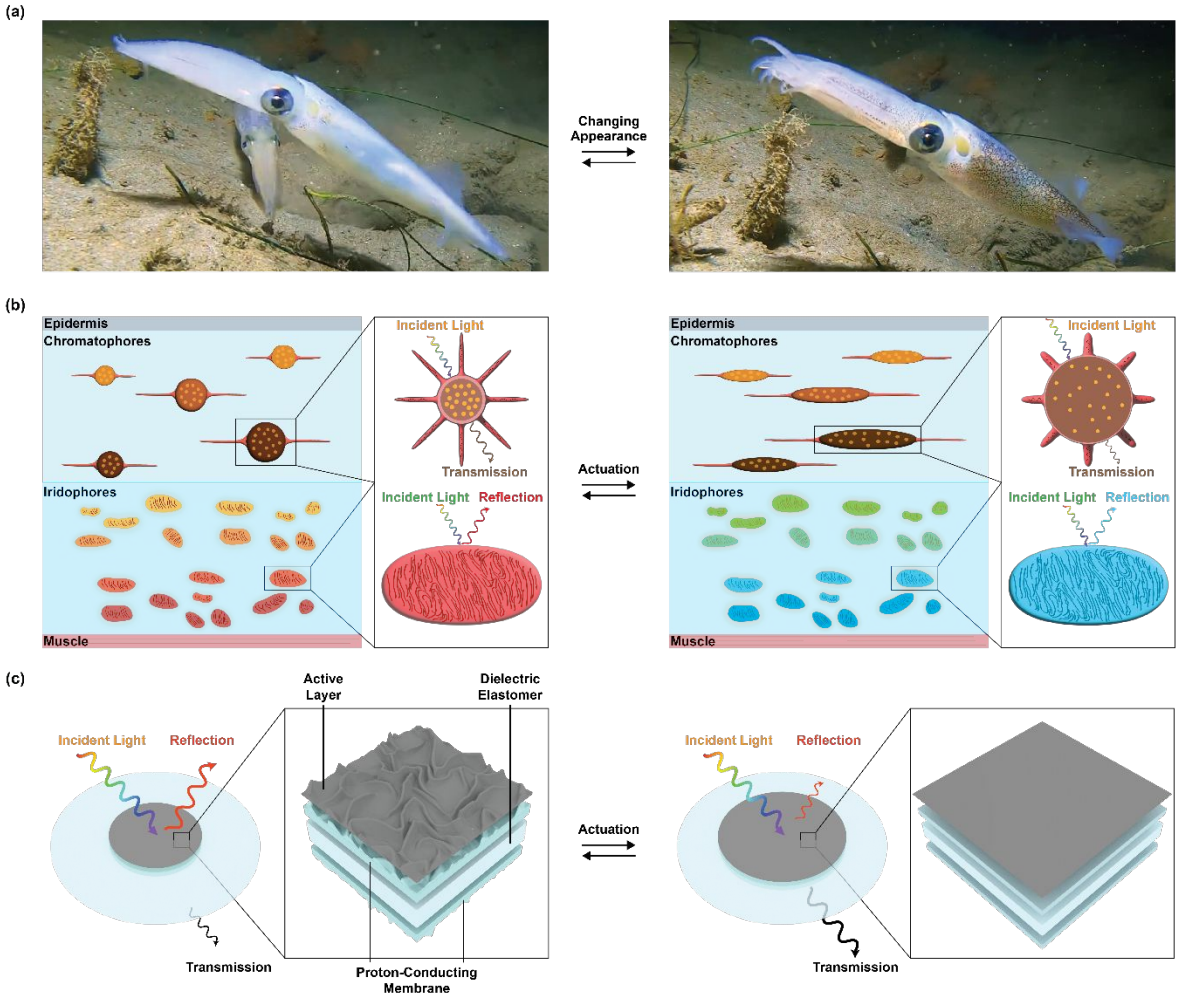

Fig. 1. Bioinspired design of ultraviolet, visible, and near-infrared camouflage systems. (a) Camera images of a common squid that changes appearance from white (left) to colored (right). **(b)** A schematic of the hierarchical architecture of squid skin containing pigmented organs called chromatophores and reflective cells called iridophores before (left) and after (right) actuation. The chromatophores modulate the transmission of light by reversibly expanding upon neuromuscular actuation (compare left to right), and the iridophores modulate the reflection of incident light by reversibly changing ultrastructure upon neurophysiological actuation (compare left to right). **(c)** A schematic of parallel plate capacitor-type devices consisting of a spectroscopically-functional active layer, a deformable dielectric elastomer membrane, and/or transparent proton-conducting

electrodes before (left) and after (right) mechanical or electrical actuation. The devices simultaneously expand their areas, reconfigure their surface microstructures, and alter their interaction with incident light upon actuation (compare left to right). Note that the images in **(a)** are reproduced from a video with permission from SD Diver Art, "California Market Squid," YouTube, https://www.youtube.com/watch?v=0DBexhP1xQE (2022), Copyright 2022, licensed under a Creative Commons Attribution license[45].

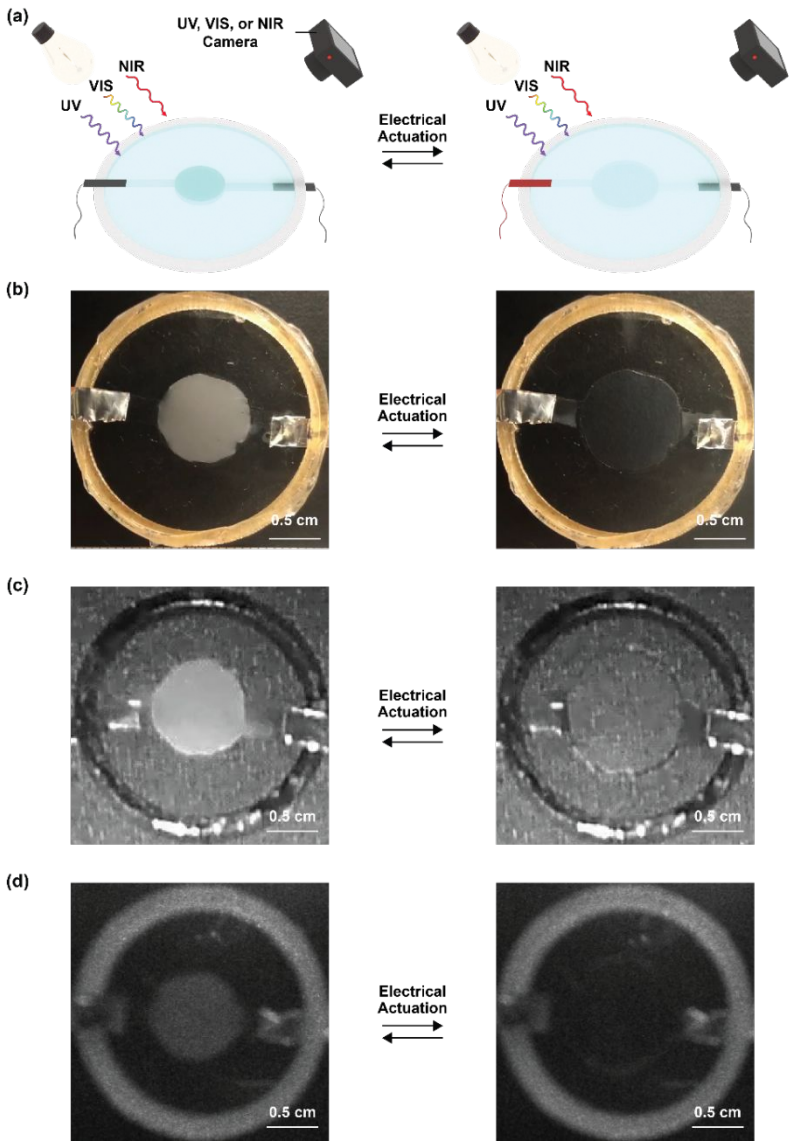

Fig. 2. Visible, ultraviolet, and near-infrared appearance-changing functionalities of small-area camouflage systems. (a) Schematic of a small-area device undergoing imaging under either visible (VIS), ultraviolet (UV), or near-infrared (NIR) light illumination during electrical actuation. **(b)** Representative digital camera images of a small-area device before (left) and after (right) electrical actuation. **(c)** Representative ultraviolet camera images of a small-area device before (left) and after (right) electrical actuation. **(d)** Representative near-infrared camera images of a small-area device before (left) and after (right) electrical actuation. The devices were actuated with square waveforms (minima at 0 kV and maxima at 3.8 kV) at a frequency of 0.05 Hz.

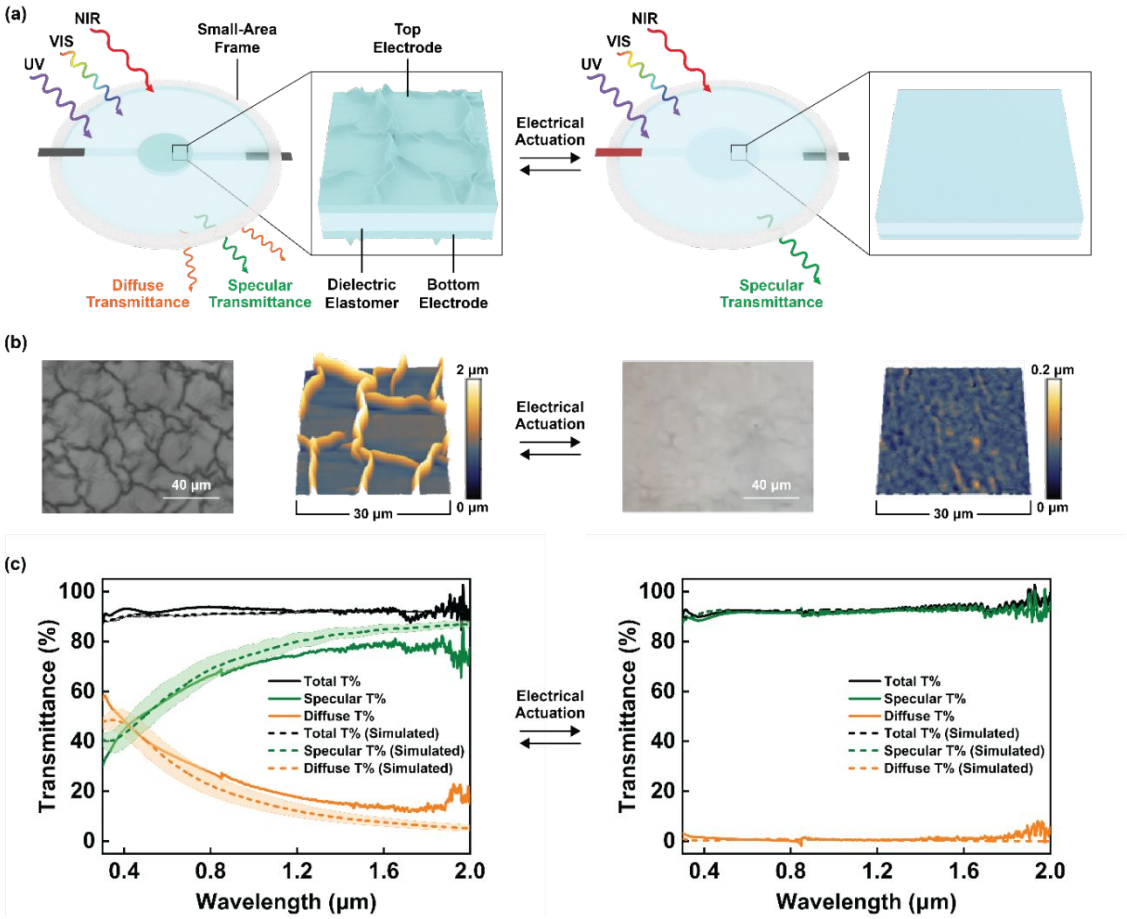

Fig. 3. Morphological and spectroscopic characterization of small-area camouflage systems. **(a)** Schematic of a small-area device for which the surface microstructure and the transmission and reflection of light both change upon electrical actuation. **(b)** Representative OM and AFM images obtained for the active regions of small-area devices before (left) and (right) electrical actuation. **(c)** Representative measured total (solid black line), specular (solid green line), and diffuse (solid orange line) transmittance spectra and representative simulated total (dashed black line), specular (dashed green line), and diffuse (dashed orange line) transmittance spectra for the small-area devices before (left) and (right) electrical actuation. The devices were actuated with a 3.8 kV step voltage at a frequency of 0.05 Hz. Note that the shaded black, green, and orange regions represent spectra simulated for the wrinkle geometries in **Table S2**.

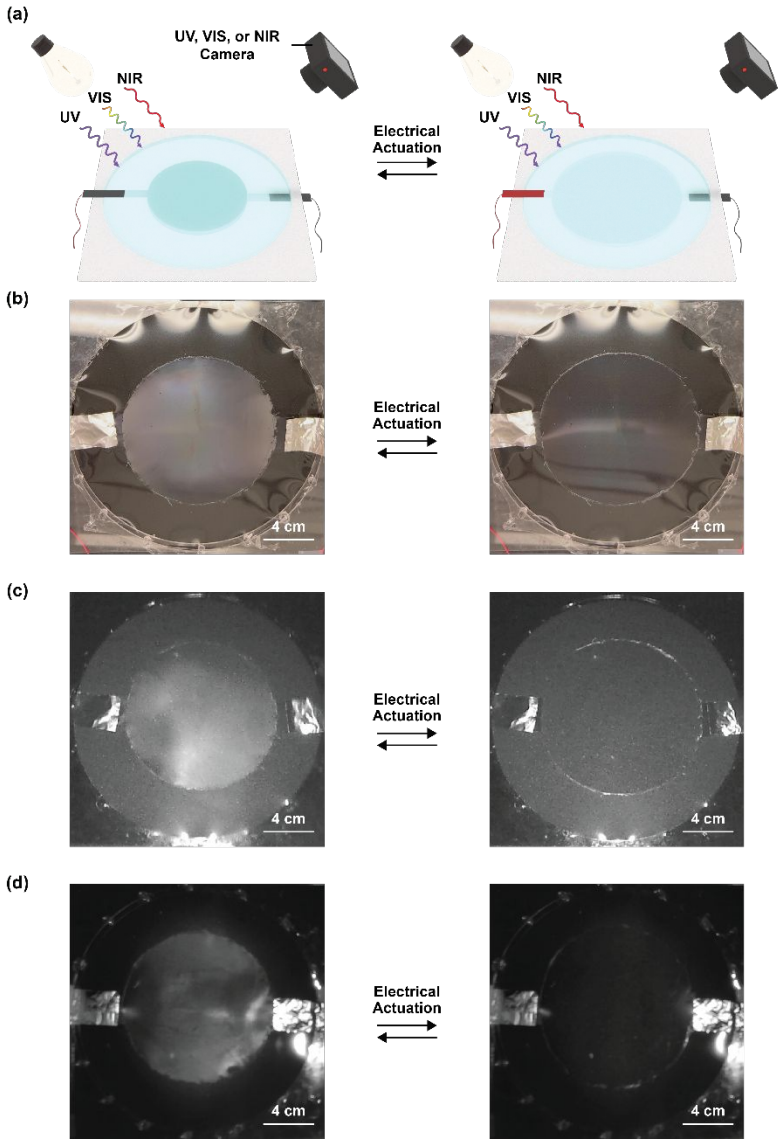

Fig. 4. Visible, ultraviolet, and near-infrared appearance-changing functionalities of large-area camouflage systems. (a) Schematic of a large-area device undergoing imaging under either visible (VIS), ultraviolet (UV), or near-infrared (NIR) light illumination during electrical actuation. **(b)** Representative digital camera images of a large-area device before (left) and after (right) electrical actuation. **(c)** Representative ultraviolet camera images of a large-area device before (left) and after (right) electrical actuation. **(d)** Representative near-infrared camera images of a large-area device before (left) and after (right) electrical actuation. The devices were actuated with square waveforms (minima at 0 kV and maxima at 3.8 kV) at a frequency of 0.05 Hz.

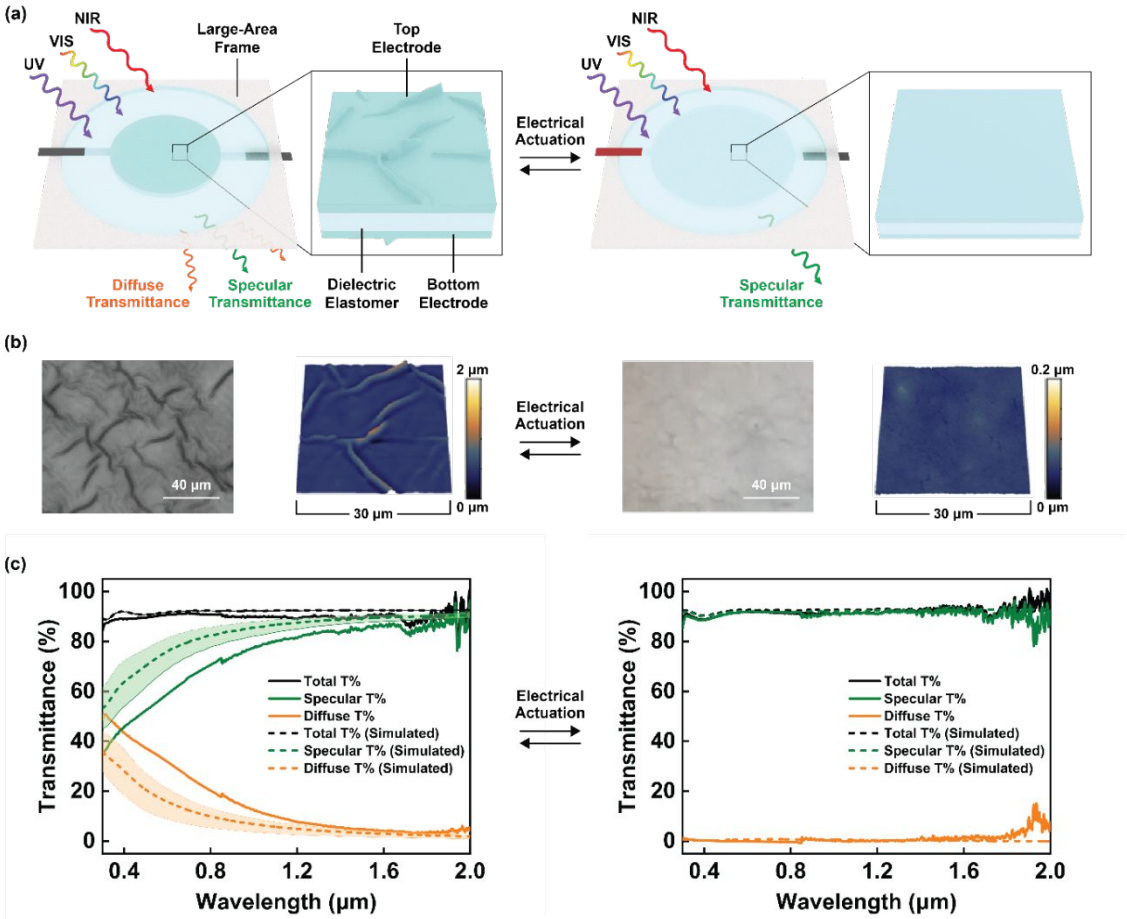

Fig. 5. Morphological and spectroscopic characterization of large-area camouflage systems. **(a)** Schematic of a large-area device for which the surface microstructure and the transmission and reflection of light both change upon electrical actuation. **(b)** Representative OM and AFM images obtained for the active regions of large-area devices before (left) and (right) electrical actuation. **(c)** Representative measured total (solid black line), specular (solid green line), and diffuse (solid orange line) transmittance spectra and representative simulated total (dashed black line), specular (dashed green line), and diffuse (dashed orange line) transmittance spectra for the large area-devices before (left) and (right) electrical actuation. The devices were actuated with a 3.8 kV step voltage at a frequency of 0.05 Hz. Note that the shaded black, green, and orange regions represent spectra simulated for the wrinkle geometries in **Table S2**.

Data Availability

The data that support the findings of this study are available within the article and its supplementary material and are available from the corresponding author upon reasonable request.